atmosphere

MDPI

Article

Assessing Satellite Data's Role in Substituting Ground Measurements for Urban Surfaces Characterization: A Step towards UHI Mitigation

Davide Parmeggiani [1,*], Francesca Despini [1], Sofia Costanzini [1], Malvina Silvestri [2], Federico Rabuffi [2], Sergio Teggi [1] and Grazia Ghermandi [1]

[1] Department of Engineering, University of Modena and Reggio Emilia, 41125 Modena, Italy; francesca.despini@unimore.it (F.D.); sofia.costanzini@unimore.it (S.C.); sergio.teggi@unimore.it (S.T.); grazia.ghermandi@unimore.it (G.G.)

[2] National Institute of Geophysics and Volcanology, 00143 Rome, Italy; malvina.silvestri@ingv.it (M.S.); federico.rabuffi@ingv.it (F.R.)

* Correspondence: davide.parmeggiani@unimore.it

Abstract: Urban surfaces play a crucial role in shaping the Urban Heat Island (UHI) effect by absorbing and retaining significant solar radiation. This paper explores the potential of high-resolution satellite imagery as an alternative method for characterizing urban surfaces to support UHI mitigation strategies in urban redevelopment plans. We utilized Landsat images spanning the past 40 years to analyze trends in Land Surface Temperature (LST). Additionally, WorldView-3 (WV3) imagery was acquired for surface characterization, and the results were compared with ground truth measurements using the ASD FieldSpec 4 spectroradiometer. Our findings revealed a strong correlation between satellite-derived surface reflectance and ground truth measurements across various urban surfaces, with Root Mean Square Error (RMSE) values ranging from 0.01 to 0.14. Optimal characterization was observed for surfaces such as bituminous membranes and parking with cobblestones (RMSE < 0.03), although higher RMSE values were noted for tiled roofs, likely due to aging effects. Regarding surface albedo, the differences between satellite-derived data and ground measurements consistently remained below 12% for all surfaces, with the lowest values observed in high heat-absorbing surfaces like bituminous membranes. Despite challenges on certain surfaces, our study highlights the reliability of satellite-derived data for urban surface characterization, thus providing valuable support for UHI mitigation efforts.

Keywords: surface reflectance; albedo; urban surfaces characterization; SUHI; spectral signature

Citation: Parmeggiani, D.; Despini, F.; Costanzini, S.; Silvestri, M.; Rabuffi, F.; Teggi, S.; Ghermandi, G. Assessing Satellite Data's Role in Substituting Ground Measurements for Urban Surfaces Characterization: A Step towards UHI Mitigation. *Atmosphere* **2024**, *15*, 551. https://doi.org/10.3390/atmos15050551

Academic Editor: Ferdinando Salata

Received: 20 March 2024
Revised: 15 April 2024
Accepted: 24 April 2024
Published: 29 April 2024

1. Introduction

The Urban Heat Island (UHI) phenomenon delineates a stark contrast in temperature between urbanized regions and their adjacent rural environs [1]. This thermal dichotomy arises from the compounding effects of urban expansion and global warming. Urban landscapes, characterized by impermeable surfaces such as concrete and asphalt, possess a heightened capacity to absorb and retain solar radiation, perpetually emitting heat both diurnally and nocturnally. In contrast, rural areas, with their prevalent vegetation and porous soils, exhibit diminished thermal retention capabilities. This disparity in thermal behavior manifests notably during nocturnal hours when urban surfaces gradually release stored heat, maintaining elevated temperatures within the urban microclimate [2]. The resultant urban heat signature often escalates temperatures by 5–10 °C relative to their rural surroundings [3]. As cities keep expanding, the UHI issue becomes increasingly concerning. Elevated urban temperatures engender multifaceted consequences, including heightened energy demands for cooling, heightened susceptibility to heat-related illnesses,

and compromised air quality [4,5]. Consequently, increased greenhouse gas emissions further exacerbate the cycle of global warming, perpetuating the UHI feedback loop.

The Surface Urban Heat Island (SUHI) phenomenon refers to increased temperatures observed in urban surfaces compared to their surrounding rural areas, and it correlates with the broader UHI effect seen in densely populated urban centers. Numerous studies have delved into quantifying the profound influence of urban expansion on urban surface temperatures and their surrounding microclimates. These investigations consistently reveal a compelling correlation between urban density and surface temperature variations within the urban fabric. Specifically, the data underscore a distinct positive relationship where heightened urban density invariably translates to elevated surface temperatures, marking a significant positive correlation with correlation coefficient higher than 0.85 [6,7]. Conversely, cities characterized by lower density and exhibiting lower temperatures (referred to as low–low) alongside a more dispersed urban layout showcase a notable cooling effect across their proximate environments. The SUHI effect is, thus, influenced by the morphological characteristics of urban areas. Non-linear random forest regression analysis further demonstrated that 91.84% of the variability in the SUHI effect can be explained by morphological factors [8,9]. These findings underscore the importance of an appropriate spatial layout for built-up areas to mitigate the SUHI effect.

In this framework, to mitigate SUHI effects, the deployment of solar reflective materials emerges as a promising technological recourse [10,11]. These materials, colloquially known as "cool roofs" or "cool pavements", augment the solar reflectance (or albedo) of urban surfaces, thereby mitigating the heat absorption literature [12,13]. Strategic application of such materials to areas with lower solar reflectance stands as a measure to yield substantial ameliorative effects [14,15]. Therefore, comprehensive urban surfaces characterization is fundamental for informed intervention strategies.

In scientific practice, the determination of radiometric properties of surfaces typically involves adherence to standardized ASTM methods. These methods employ a range of instruments tailored to specific standards. Notable instruments include a spectrophotometer equipped with a 150 mm integrating sphere spanning wavelengths from 300 to 2500 nm, a reflectometer, and a pyranometer [16]. These instruments are detailed in ASTM standards such as ASTM E903, ASTM C1549, and ASTM E1918, respectively [17,18]. Another valuable tool in this context is the ASD Fieldspec 4, a field spectroradiometer that delivers highly accurate measurements of solar reflectance values across a broad spectral range spanning from 350 to 2500 nm [19].

However, these instruments provide measurements in specific points, and may not be suitable for assessing extensive areas. For this purpose, remote sensing emerges as an important and practical tool for analyzing and characterizing large urban areas [20]. Through satellite imagery equipped with Thermal InfraRed (TIR) bands, it becomes possible to compute Land Surface Temperature (LST) and identify hotspots and critical areas within urban environments [21]. Moreover, satellite sensors with bands in the Visible and Near Infrared spectral regions enable the extraction of key surface characteristics, such as solar reflectance (or albedo), which represents the proportion of solar radiation reflected back into the atmosphere [22].

Hence, two pivotal questions arise: "Are satellite remote sensing measurements consistent with ground-based measurements?" and "Can satellite measurements be effectively used to characterize surface conditions, thus replacing laboratory measurements?" This paper aims to tackle these inquiries by scrutinizing disparities and correlations between surface reflectance spectra detected remotely and ground measurements. Specifically, our analysis harnesses remote sensing data acquired from the WorldView3 satellite sensor alongside ground measurements from the Jasco V-670 UV-Vis-NIR laboratory spectrophotometer (Jasco International, Tokio–Japan, equipment provided by EElab laboratory, University of Modena) equipped with a 150 mm integrating sphere covering wavelengths from 300 to 2500 nm, as well as the ASD FieldSpec 4 field spectroradiometer (Malvern Panalytical, Cambirisge–UK, equipment provided by National Institute of Geophysics and Volcanology)

spanning wavelengths from 350 to 2500 nm. This integrated methodology allows for the characterization of urban surfaces in terms of their spectral signatures and albedos using satellite imagery.

The study area is the Municipality of Sassuolo, located in the northern part of Italy, where several Regions of Interest (ROIs) have been selected as test sites for comparison. The chosen ROIs represent the prevalent impervious urban surfaces found within the study area, as well as more broadly across urban environments.

Furthermore, we have acquired and analyzed a comprehensive time series of Landsat images to evaluate the temporal trend of LST specifically on urban impervious surfaces. Our emphasis on these surfaces stems from their amenability to replacement with solar reflective materials, thereby playing a pivotal role in mitigating the SUHI effect.

Additionally, the nearest LST map produced for the year of the WV3 satellite image acquisition has been examined and compared to the albedo map to identify the correspondence between critical areas, hotspots, and areas with low albedo values.

With these analyses, our aim is to ascertain the satellite data's efficacy in characterizing surfaces comparably to laboratory or on-field measurements. This enables swift and facile identification of potential critical areas within urban zones where UHI effects are most prominent. Subsequently, it facilitates the exploration of mitigation strategies that may include the strategic deployment of solar reflective materials in areas significantly affected by the phenomenon.

2. Materials and Methods

2.1. Study Area

The study area of this study is the municipality of Sassuolo, situated within the Emilia-Romagna region in northern Italy. Sassuolo is part of the Emilian ceramic district, alongside neighboring municipalities such as Fiorano Modenese, Maranello, Casalgrande, and Formigine. The choice of this area is due to the highly urbanized and industrialized urban fabric. Located within the Po Valley, this geographical region is characterized by subdued or near-absent winds due to the surrounding mountainous terrain. Consequently, heat emissions from urban surfaces tend to remain localized, with limited dispersion to adjacent areas via advective processes [23]. This restricted dissipation of heat contributes to heightened air temperatures within the city, leading to the emergence of the UHI phenomenon. Furthermore, the lack of strong winds poses challenges for air quality management, as pollutants accumulate more readily in urban environments [24]. Figure 1 shows the location of the study area.

2.2. Dataset

Initially, we acquired a Worldview3 (WV3) image of the study area. This image served as the basis for extracting spectral signatures and determining the albedo of urban surfaces within our scope of interest. Additionally, it allowed us to compare these measurements with those obtained through fieldwork and laboratory analysis.

The WV3 satellite sensor is equipped with 16 multispectral bands, comprising 8 bands in the Visible-Near Infrared (VNIR) range and 8 in the Short Wave Infrared (SWIR) range. The spectral resolution of these bands is, respectively, 1.20 m and 7.50 m. Detailed specifications of the WV3 sensor bands are provided in Table 1. Primarily, the selection of the WV3 image was guided by prudent resource management, considering the substantial costs typically associated with acquiring high-resolution satellite imagery, particularly for expansive study domains. Moreover, the availability of the WV3 image from a previous research endeavor expedited our project timeline and minimized acquisition-related expenditures.

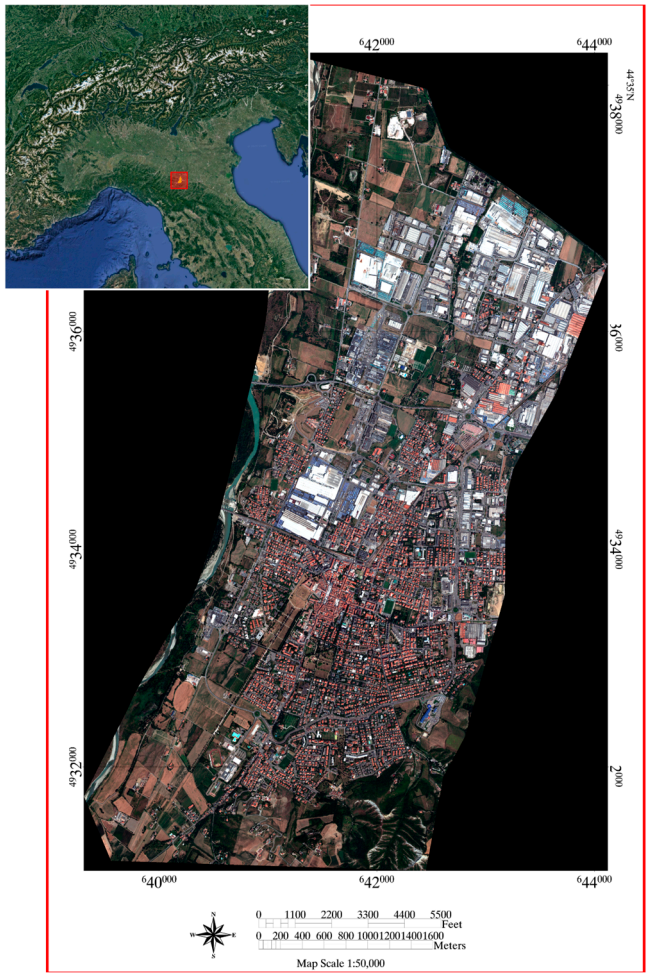

Figure 1. Location of the study area.

Table 1. Satellite specifics of WorldView3.

Spectral Region	Bands	Bandwidth (nm)	Spatial Resolution (m)
Visible—Near Infrared	Coastal—blue	400–450	1.20
	Blue	450–510	
	Green	510–580	
	Yellow	590–630	
	Red	630–690	
	Red-edge	710–750	
	NIR-1	770–900	
	NIR-2	860–1040	
Short wave Infrared	SWIR-1	1120–1230	7.50
	SWIR-2	1550–1600	
	SWIR-3	1640–1680	
	SWIR-4	1710–1750	
	SWIR-5	2150–2190	
	SWIR-6	2190–2230	
	SWIR-7	2240–2290	
	SWIR-8	2240–2370	

The image of the study area was captured on 31 July 2018 at 10:30 am, coinciding with the passage of the WV3 sensor over the study area (Figure 2). The timeliness of the image ensured a precise representation of the study area's current characteristics, encompassing pertinent urban surface attributes crucial to our analytical pursuits.

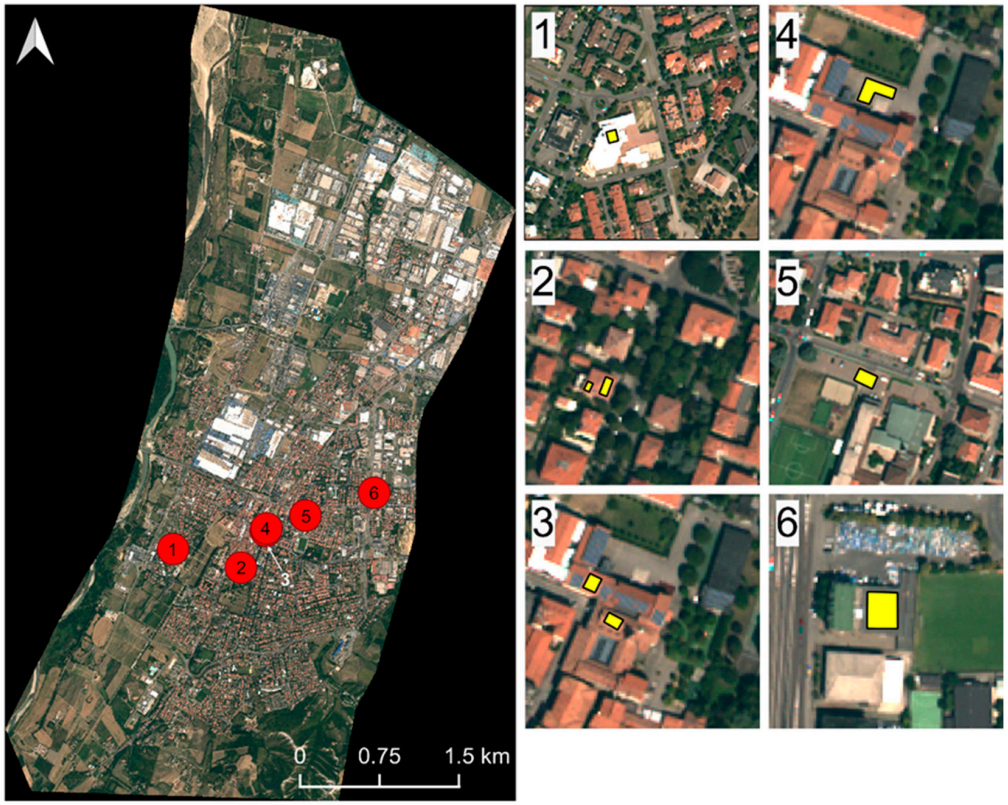

Figure 2. WorldView3 image of the study area and overlook of the chosen ROIs highlighted in yellow. 1: Polyolefin roof, 2: new tiles roof, 3: aged tiles roof, 4: asphalt parking, 5: parking with cobblestones, 6: bituminous membrane.

In addition to covering the municipality of Sassuolo, the image encompasses neighboring municipalities, which will be instrumental in extending our study to the entire Emilian ceramic district. While our initial study was limited to utilizing the image solely for the Sassuolo municipality, the surfaces studied are nearly identical throughout the entire Emilian ceramic district. Therefore, any expansion of the study will likely involve classifying the entire district, although the surfaces under analysis will remain consistent with the current study.

Given the subject matter under investigation, we directed our attention towards the most urbanized part of the Municipality of Sassuolo, omitting the hilly areas that were not pertinent to our study.

Furthermore, Landsat 5, 7, and 8 images have been used to retrieve LST maps and statistics on the study area. Landsat 5, launched in 1984, operated until its retirement in 2013. Equipped with the Thematic Mapper (TM) sensor, Landsat 5 provided data with seven spectral bands covering a range from visible to thermal infrared. Its spatial resolution was typically 30 m for most bands, with a resolution of 120 m for the thermal band [25]. Following Landsat 5, Landsat 7 was launched in 1999, featuring the Enhanced Thematic Mapper Plus (ETM+) sensor. This sensor enhanced the capabilities of Landsat imaging, offering similar spectral bands to Landsat 5, but with improved radiometric and geometric characteristics [26]. In 2013, Landsat 8 continued the legacy of its predecessors, equipped with the Operational Land Imager (OLI) and Thermal Infrared Sensor (TIRS). Landsat 8's OLI sensor provides data with nine spectral bands, including improved spectral resolution compared to previous sensors, while the TIRS sensor captures thermal infrared data with two bands [27]. Overall, Landsat satellites have played a crucial role in monitoring land use, land cover changes, environmental studies, and various other applications contributing valuable data to scientists, researchers, and policymakers around the world [28].

Utilizing Landsat imagery, we calculated the median LST for the meteorological summer, spanning from June to August, for each year from 1985 to 2023. Additionally, we computed the maximum and minimum temperature values for each year during the summer period. The analysis of these values offers insights into the SUHI phenomenon, closely associated with the development of the UHI phenomenon [29,30].

2.3. Ground Truth Data

For ground-based measurements, the ASD FieldSpec 4 pro portable spectroradiometer was used to measure solar reflectance directly on field [19]. FieldSpec is a field portable radiometer designed for rapid data collection, capable of capturing spectra in just 1/10th of a second. It is specifically engineered to gather measurements of solar reflectance, radiance, and irradiance. Three distinct spectrometers cover the spectral range from 350 to 2500 nm, with one operating in the Visible and Near-Infrared (VNIR) region and two in the Short-Wave Infrared (SWIR) region. The sampling rate is 0.2 s per spectrum [19]. Measurements were conducted using the fiber-optic cable, featuring a field of view of 25°, with a portable Garmin GPS recording the coordinates for each spectrum in NMEA format. The instrument is equipped with an internal calibration system, allowing for the calibration operations to be performed typically during optimization at each measuring cycle or in response to variations in environmental conditions. Acquisition instrument procedures are managed with a laptop, which enables the measurement of dark power and the configuration of the capture mode for radiance or reflectance. Technical specifications of the instrument are reported in Table 2.

Table 2. Technical specifications of the ASD FieldSpec 4 Standard Resolution [19].

Spectral Range	350–2500 nm
Spectral Resolution	3 nm @ 700 nm 10 nm @ 1400/2100 nm
Sampling Interval *	1.4 nm @ 350–1050 nm 2 nm @ 1000–2500 nm
Scanning Time	100 milliseconds
Stray light specification	VNIR 0.02%—SWIR 1 & 2 0.01%
Wavelength reproducibility	0.1 nm
Wavelength accuracy	0.5 nm
Maximum radiance **	VNIR 2 × Solar—SWIR 10 × Solar
Bands	2151

* The symbol "@" is used here to denote the relationship between spectral resolution and a specific wavelength. ** Maximum radiance measurements are expressed as multiples of solar irradiance: VNIR (2 times Solar), SWIR (10 times Solar).

The initial aim of the study was to compare all field measurements, along with satellite data, to laboratory measurements obtained using the Jasco V-670 UV-Vis-NIR spectrophotometer. This instrument was enhanced with an additional 150 mm integrating sphere (ILN 725 model), covering the spectral range from 300 nm to 2500 nm [16]. However, the instrument requires a sample of urban surfaces for analysis, which proved challenging to obtain for the types of surfaces under study. Consequently, the analysis with the spectrophotometer was restricted to the bituminous roof surface identified within the urban area of Sassuolo, for which a sample for measurement was available.

2.4. Regions of Interest Identification

For comparing spectral signatures and albedo acquired from satellite and ground-based measurements, a suitable number of ROIs were carefully selected to enable the study of diverse urban surface types. These ROIs were chosen based on their internal homogeneity and the uniformity of their immediate surroundings. Additionally, criteria

such as consistent lighting conditions and a size exceeding 16 m^2 were followed to ensure compatibility with the 7.50 m resolution in the SWIR region of the satellite image.

Six ROIs were acquired from the satellite and with specific ground measurements using the FieldSpec spectroradiometer (Figure 2).

This selection was underpinned by the overarching goal of ascertaining whether satellite-derived data can effectively capture reflectance patterns in a manner comparable to ground-level measurements. To achieve this objective, a spectrum of typical urban surfaces was identified, leading to the following designated areas:

- Polyolefin roof.
- Aged tiles roof.
- New tiles roof.
- Asphalt parking.
- Bituminous membrane.
- Parking with cobblestones.

This selection of surfaces seeks to encapsulate a diverse range of materials and textures commonly encountered within the study region. The study area was intentionally chosen to encapsulate prevailing conditions found in analogous locales.

The primary objective centers around evaluating the capacity of satellite data to accurately depict the reflectance properties of these surfaces vis à vis in situ measurements facilitated by using the FieldSpec spectroradiometer.

The choice of six ROIs was deliberate and aligned with several key considerations integral to the study's objectives.

Firstly, it is important to note that for each ROI, at least 10 measurements were taken using the FieldSpec spectroradiometer, and the average spectrum was derived. This approach ensured robust data collection and representative spectral signatures for analysis. Furthermore, the selection of ROIs was based on the most common urban materials found not only within the study area, but also across Italy, ensuring broader applicability and relevance. The chosen materials represent surfaces commonly encountered in urban settings, and are potential candidates for replacement with solar reflective materials to increase surface albedo and mitigate the UHI effect. Therefore, characterizing these specific material types was crucial to evaluating their reflectance properties and potential for mitigation strategies. In essence, while the number of ROIs may seem limited, their selection and characterization were meticulously planned to serve the specific goals of the study, including representativeness, practical applicability, and relevance to broader urban contexts beyond the study area.

It is important to note that, despite the careful selection of ROIs, some complex surfaces may present additional challenges in remote characterization. These difficulties may stem from reflectance variation due to different atmospheric conditions, cast shadows, and material complexity. Although such challenges were not discussed in detail in this study, they are relevant topics deserving further exploration and discussion. However, for the purposes of this study, the studied surfaces did not exhibit these complexities, and therefore the procedures were not hindered by such issues.

2.5. Methodology

The methodology employed in this study is illustrated in Figure 3, which provides a comprehensive chart depicting the sequential steps followed in data collection, processing, and results.

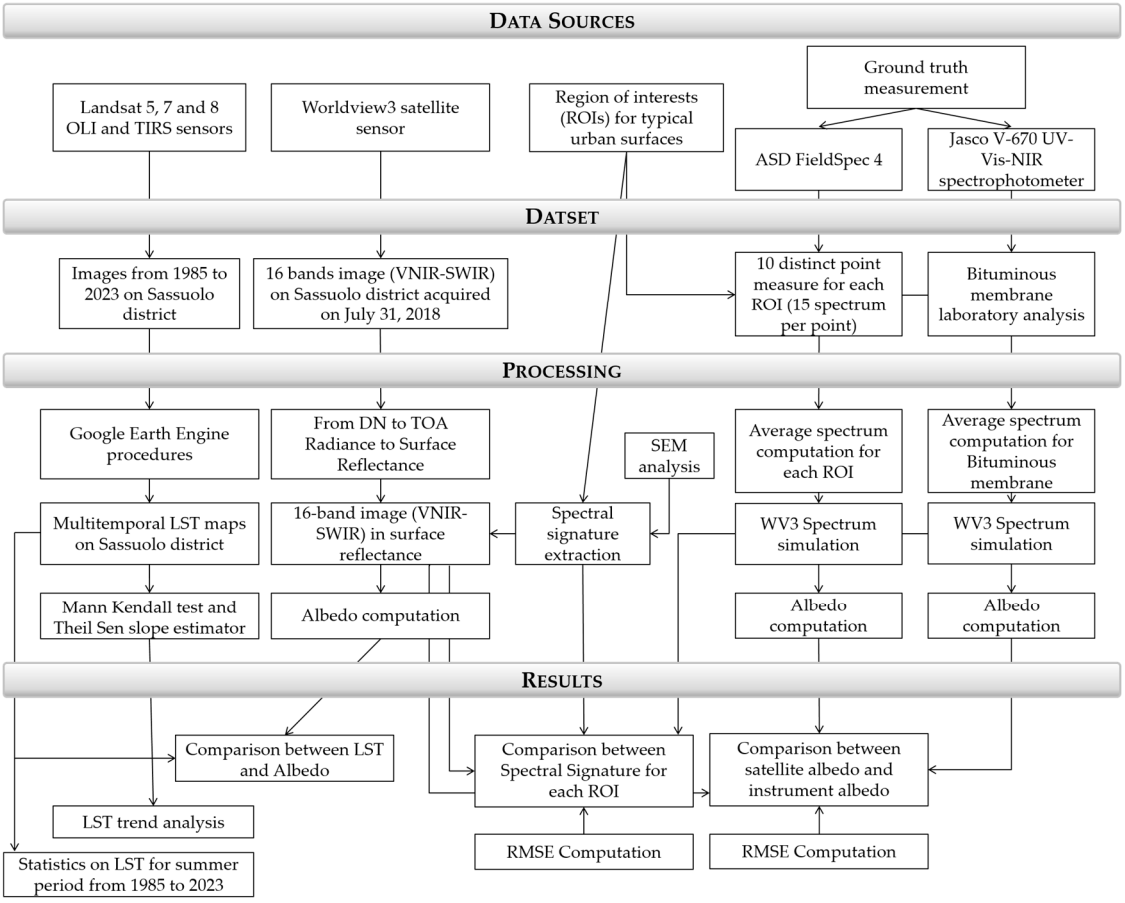

Figure 3. Methodology chart.

2.5.1. Satellite Images

The Landsat 5, 7, and 8 images spanning from 1985 to 2023 were processed using the open-source platform Google Earth Engine. We utilized datasets comprising atmospherically corrected surface reflectance and land surface temperature, derived from data generated with Landsat 5, 7, and 8 satellites. Pre-processing operations on these datasets merely necessitated the application of scale and offset factors as indicated in the metadata, along with the implementation of a masking function to exclude images with excessively high cloud cover, ensuring their suitability for analysis. For each year, the median LST over the area of interest (the municipality of Sassuolo) was calculated for the summer period [31]. Additionally, we computed maximum and minimum temperatures within the study area, referencing the highest and lowest values found within individual pixels rather than across the entire area. This approach allows us to identify temperature hotspots and understand the range of temperature variability present in the dataset.

In our analysis, we also applied the Mann–Kendall test and Theil–Sen slope estimator to evaluate the trend in LST over the summer period from 1985 to 2023. The Mann–Kendall test is a non-parametric statistical method used to assess trends in time-series data. It is particularly useful for detecting monotonic trends, which are trends that consistently increase or decrease over time [32]. The test provides several key statistics, including the tau statistic and the *p*-value. The tau statistic measures the strength and direction of the trend, where positive values indicate an upward trend and negative values indicate a downward trend. The *p*-value assesses the statistical significance of the observed trend. Additionally, we calculated the slope of the trend with the Theil–Sen estimator [33], which represents the rate of change in LST over time. The Theil–Sen slope estimator is a more viable alternative to a standard linear regression slope [34]. This slope provides valuable insight into the magnitude of the trend and allows us to quantify the expected change in

LST over a given period. The non-parametric Mann–Kendall and Theil–Sen slopes have been employed by various authors in the last two decades to detect the monotonic trends in a series of environmental, metrological, or hydrological data [35].

Landsat images also enable the generation of point maps of LST, which can be utilized to pinpoint hotspots or critical areas. Given the acquisition date of the WV3 image, we opted to employ the LST map from the summer of 2018 acquired on the 1st of August, to identify potential correlations between areas experiencing high temperatures and those exhibiting low albedo values.

The WV3 image acquired of the study area is provided in Digital Number (DN); thus, an initial pre-processing was needed to retrieve surface reflectance. First of all, the radiometric corrections were performed to obtain the Top of Atmosphere (TOA) radiance for each pixel. Then, the acquired image underwent atmospheric corrections to attain surface reflectance. Atmospheric corrections were imperative to mitigate signal distortions induced by atmospheric conditions. To implement atmospheric corrections, we employed the ENVI 5.3 software [36] along with the FLAASH (Fast Line of sight Atmospheric Analysis of Hypercubes) module. FLAASH harnesses the MODTRAN4 code to simulate the complex radiative transfer processes occurring within the atmosphere, which can distort surface signals. Moreover, FLAASH accounts for various factors such as adjacency effects, climatic conditions, solar positioning, atmospheric dust, and water vapor content, ensuring accurate corrections.

Following the pre-processing stage, a 16-band image in surface reflectance was obtained. This image primarily served to extract spectral signatures from the chosen ROIs and compare them with satellite measurements. Additionally, the 16 bands were utilized for albedo calculations using the methodology delineated by Kuester [37], with coefficients derived from Thuillier [38]. Prior to this procedure, albedo calculation involved complex integration of the bidirectional hemispherical reflectance distribution function [39]. However, adopting the methodology outlined by Kuester streamlines the albedo calculation process, making it faster and simpler. Presently, Thuillier coefficients are employed for sensor calibration by WV3 manufacturers [40].

The albedo value could therefore be computed using the following equation:

$$\text{Albedo} = \sum_{i=1}^{16} w_i * \rho_i \quad (1)$$

where w_i are coefficients from Thuillier [38], representing the ratio of extraterrestrial solar irradiance within the specific band to the total irradiance obtained by summing across all bands. The values for the 16 bands in the image are outlined in Table 3. Additionally, ρ_i represents the spectral reflectance for each WV3 band.

2.5.2. Ground Truth Data

The instruments utilized for ground truth data, namely the spectroradiometer and the spectrophotometer, provide spectral signatures of the investigated surface as measurement outputs. The ASD FieldSpec 4 spectroradiometer was employed to capture spectral signatures of selected ROIs at ground level (see Figure 4). The ASD FieldSpec 4 spectroradiometer was utilized for each ROI, capturing measurements at 10 distinct points within the ROI to encompass the area captured by the satellite. At each measurement point, 15 spectra were collected and subsequently averaged, with the exclusion of any measurement errors or outliers.

Table 3. Thuillier coefficient values for each WV3 sensor band.

Bands	Thuillier Coefficients (-) *
Coastal (B1)	0.13
Blue (B2)	0.15
Green (B3)	0.13
Yellow (B4)	0.13
Red (B5)	0.11
Red-edge (B6)	0.10
NIR1 (B7)	0.078
NIR2 (B8)	0.063
SWIR1 (B9)	0.035
SWIR2 (B10)	0.019
SWIR3 (B11)	0.017
SWIR4 (B12)	0.015
SWIR5 (B13)	0.0067
SWIR6 (B14)	0.0063
SWIR7 (B15)	0.0057
SWIR8 (B16)	0.0050

* The symbol (-) denotes a dimensionless parameter.

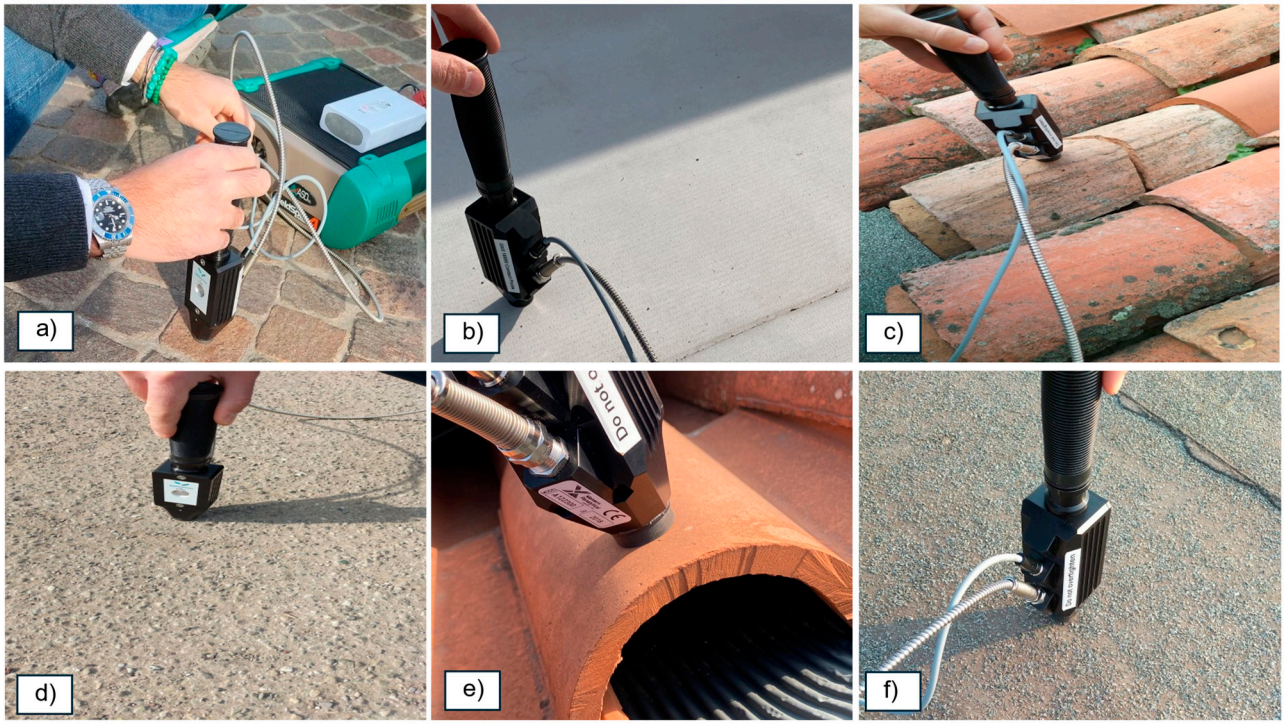

Figure 4. ASD FieldSpec 4 acquisition. (**a**) Parking with cobblestones, (**b**) polyolefin roof, (**c**) aged tiles roof, (**d**) asphalt parking, (**e**) new tiles roof, (**f**) bituminous membrane.

The laboratory spectrophotometer was used exclusively to obtain spectra from available samples of bituminous membranes.

The ground measurement campaign took place during the summer of 2023, which occurred at a different timeframe compared to the WV3 image acquisition in July 2018. Therefore, we expect to observe variations in the results attributable to surface aging processes occurring between 2018 and 2023.

The parameter of albedo, or solar reflectance, is computed using Equation (2) according to the standard method prescribed by ASTM E903-96:

$$\rho_{sol} = \frac{\sum_{i=1}^{N} [\rho(\lambda_i) * E(\lambda_i)] * \Delta\lambda_i}{\sum_{i=1}^{N} E(\lambda_i) * \Delta\lambda_i} \quad (2)$$

where:

- ρsol is the urban surface solar reflectance [-];
- $\rho(\lambda_i)$ is the urban surface spectral reflectance [-];
- $E(\lambda_i)$ is the solar spectral irradiance [W m^{-2}];
- $\Delta\lambda_i$ is the wavelength step [nm].

The $\rho(\lambda_i)$ values are acquired through measurements conducted using both the spectroradiometer and the spectrophotometer. For each instrument, ρsol is derived utilizing the standard irradiance spectrum E891BN and the AM1GH spectrum, the latter being employed to simulate high-temperature conditions. It is worth noting that $\Delta\lambda_i$ varies between the two instruments: 1 nm for the spectroradiometer, and 5 nm for the spectrophotometer.

To ensure a direct comparison between the spectral signatures of ROIs obtained from satellite and ground measurements, spectral resampling was conducted. This process is essential for aligning the spectral resolution of both datasets. The high spectral resolution of the spectroradiometer and spectrophotometer provides a comprehensive spectral library of the analyzed ROIs. This spectral information is utilized for spectral resampling, requiring the knowledge of the response function F(λ) for each satellite band. The resampling process involves applying weights to the spectral reflectance for each wavelength interval to obtain reflectance values in satellite bands. This is calculated using the formula:

$$\rho_b = \frac{\sum_{i=1}^{N} \phi_i * \rho_i}{\sum_{i=1}^{N} \phi_i} \quad (3)$$

where N represents the 16 WV3 satellite bands and Φ are the weights to be applied for each band. Each band's wavelength interval is discretized, and for each band (denoted by subscript i), the response function value Φ_i and the spectral library value ρ_i are divided by Φ_i. Consequently, ρ_b is obtained by computing a weighted average.

As mentioned before, the study aimed to compare field and satellite measurements with laboratory data obtained using the Jasco V-670 UV-Vis-NIR spectrophotometer, but, due to challenges in obtaining suitable urban surface samples for analysis, this analysis was limited to the available sample from the bituminous roof surface in Sassuolo's urban area.

3. Results and Discussion

3.1. LST Analysis

To comprehensively analyze the SUHI trends within the study area, our initial step involves examining the temporal variations of LST using Landsat 5, 7, and 8 imagery. This is depicted in Figure 5, illustrating the median, maximum, and minimum LST values during the summer period from 1985 to 2023. It is worth noting that the median LST value is calculated across the entire study area, providing an overview of the overall temperature trends. Meanwhile, the maximum and minimum LST values are calculated for the pixel with the highest and lowest temperatures recorded each year during the summer period, offering insights into localized temperature extremes. This visualization highlights the temporal variations of LST, shedding light on the magnitude and temporal patterns of SUHI over the specified time frame. To ensure a robust representation of all years within the considered period, years with only one available image for the summer period were excluded from the analysis. Figure 5 also displays the number of available images for each year. The years excluded from the study were then 1999, 2006, 2007, and 2008.

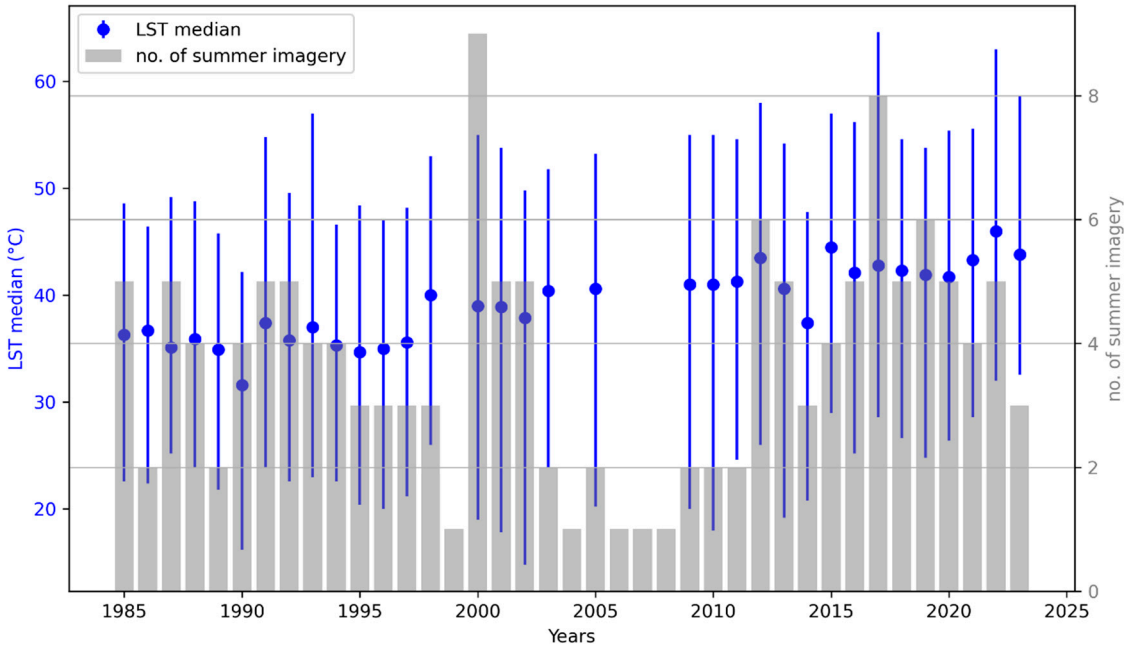

Figure 5. Median, maximum, and minimum LST values for summer period from 1985 to 2023, and number of available summer images.

Figure 5 illustrates the rising temperatures in the study area, particularly in recent years, attributable in part to the phenomenon of global warming, as well as the ongoing urbanization of the region. Analysis of land use data provided by the Emilia Romagna Region reveals a notable increase in the percentage of land consumption for the Municipality of Sassuolo, reaching 30.71% by 2022. Based on available data, starting from 2006, the net increase in land consumption has exceeded 50 hectares [41]. This upward trend underscores the impact of urban expansion on local temperature dynamics, highlighting the interplay between environmental factors and anthropogenic activities. These results are consistent with the scientific literature, where several studies have been addressed to understand the relationship between urban density and LST when computed with multitemporal Landsat imagery [6,42]. The literature analysis revealed a positive correlation between higher temperatures and levels of urban growth, with a quadratic relation for daytime and a coefficient of determination r^2 around 0.98–0.99 that decreased to 0.95–0.96 for nighttime [6,43]. Areas characterized by high-rise structures and economic activities experienced the most pronounced impact of the heat island phenomenon [44,45].

The median LST ranges from a minimum of 31.6 °C to a maximum of 46.0 °C. The peak values are observed in the years following 2000, with the highest median LST recorded in 2022. It is important to note and emphasize that Landsat images are acquired around 10 am, when urban surfaces are still absorbing heat, and certainly do not reflect the peak temperatures of the day.

Looking at median LST, the results obtained from the Mann–Kendall test reveal compelling evidence of a significant positive trend over the analyzed period. The tau statistic of 0.67 and the low p-value of 2.26×10^{-8} indicate a robust and consistent upward trend in LST. Moreover, the calculated slope of 0.292 further confirms the magnitude of this trend. This slope represents the rate of change in LST over time. Specifically, it implies that if the current trend continues, we can expect an increase of 2.92 °C in LST over ten years. This trend is deemed significant at the 99% confidence level, suggesting a high level of certainty in the observed increase in LST. The obtained trend is consistent with the literature studies that found, in several worldwide locations, values from 0.017 to 0.32 °C [46,47].

We also aimed to obtain a comprehensive overview of the relationship between temperature hotspots and albedo, which is a key parameter for its influence on the distribution and intensity of the SUHI phenomenon. Thus, we decided to focus only on impervious

surfaces given the well-known negative correlation between LSTs and albedos in these kind of surfaces (for vegetation, we need to consider the evapotranspiration process as well), which has already been investigated in several studies [48,49]. Figure 6 shows the LST map of 1 August 2018, clipped on anthropic impervious surfaces retrieved from the Corine Land Cover map of 2017 [50] of the Emilia Romagna region. Side by side, we report the WV3 surface reflectance image represented in natural colors to highlight how LSTs in the southern residential area are lower than those in the northern industrial area, where LST peaks reach up to 52 °C. To correlate LST with different types of urban surfaces, Figure 6 also includes the albedo map from the WV3 image that highlights critical areas in the industrial zone, where low albedo values correspond to high LSTs.

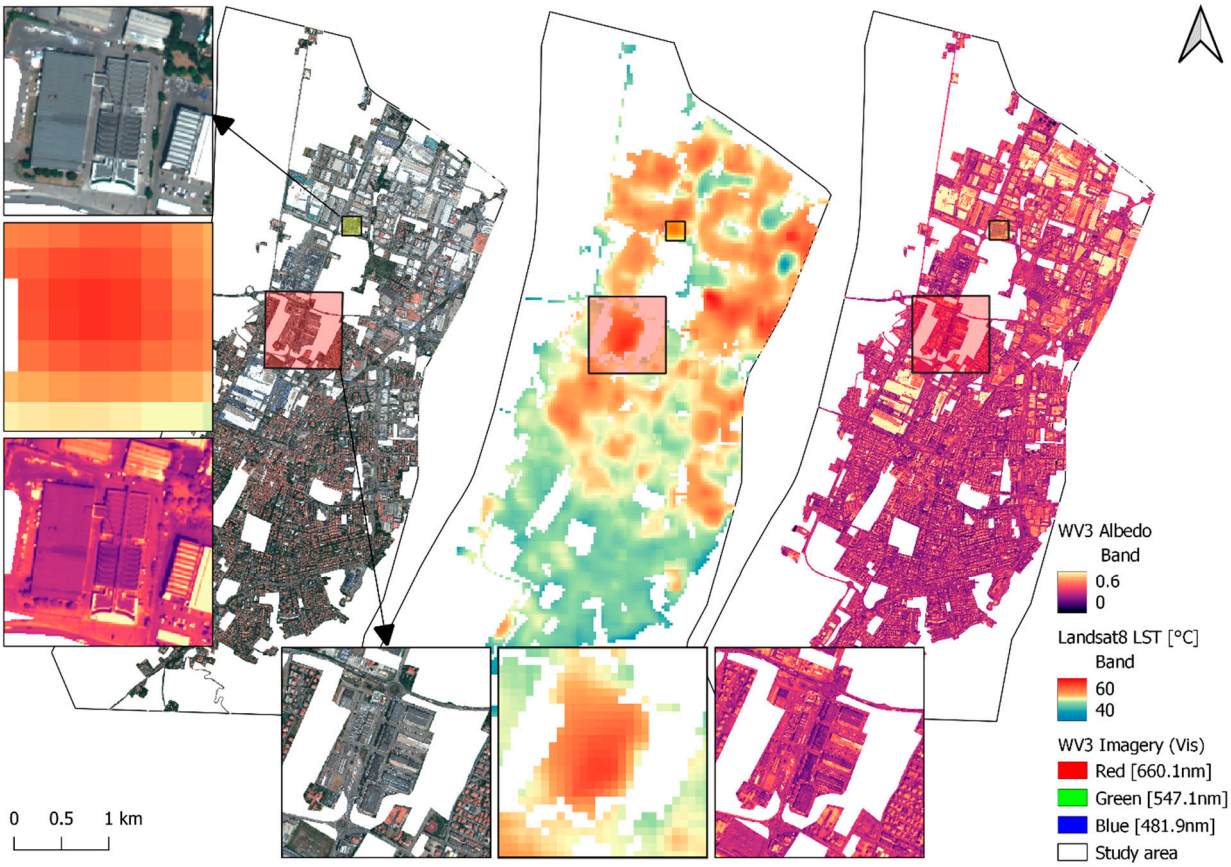

Figure 6. WV3 image (**left**), LST map [°C] (**center**), and albedo map (**right**) of the study area. Boxes highlighted and depicted in the figure with zoom are used to visualize critical areas.

The negative correlation between LST and albedo, as illustrated in Figure 6, unveils crucial insights into the SUHI phenomenon and mitigation strategies. Areas exhibiting high LST and low albedo values indicate surfaces that absorb more solar radiation, contributing significantly to localized heat buildup. Understanding this relationship offers opportunities for proactive urban planning and sustainable development practices [48].

High LST coupled with low albedo areas represent urban heat hotspots, intensifying the UHI effect. These regions experience elevated temperatures, impacting human health, energy consumption for cooling, and overall urban microclimate quality [4]. The concentration of such heat-prone zones highlights areas requiring targeted interventions to reduce thermal stress and enhance urban livability.

Identifying surfaces with low albedo and high LST not only helps understand the exacerbation of the SUHI phenomenon, but also guides interventions using high albedo solar-reflective materials. Implementing cool roofs, reflective pavements, green infrastructure, and urban forestry in these zones can mitigate heat absorption, lower surface

temperatures, and reduce energy demands for cooling buildings [51]. These measures not only enhance local thermal comfort, but also promote energy efficiency and sustainability in urban environments.

Insights from the LST–albedo relationship guide urban planners, policymakers, and stakeholders in prioritizing UHI mitigation efforts. Integrating heat mitigation strategies into urban design standards, zoning regulations, and building codes can foster climate-resilient cities [52].

3.2. Spectral Analysis

Initially, the standard error of the mean (SEM) was calculated for WV3 imagery to assess the homogeneity of the selected ROIs. The SEM provides insights into the variability of sample means around the population mean, aiding in the determination of whether the chosen ROIs exhibit uniform characteristics or not.

In particular, the SEM measures the precision of the sample mean estimate as an approximation of the population mean. It quantifies the dispersion or variability of sample means around the population mean. The SEM is calculated by dividing the population standard deviation by the square root of the sample size. It provides important information about the accuracy of the sample mean in representing the population mean, taking into account sample variability and sample size.

The formula for calculating the SEM is:

$$\text{SEM} = \frac{\sigma}{\sqrt{n}} \tag{4}$$

where:

- SEM is the standard error of the mean;
- σ is the population standard deviation;
- n is the sample size.

Researchers often use SEM to assess the reliability and precision of sample means in estimating population parameters. A smaller SEM indicates greater precision, meaning that the sample mean is a more accurate representation of the population mean.

Table 4 shows SEM values computed for each ROI and for each WV3 band. For the VNIR bands, surfaces such as Bituminous membrane, Parking with cobblestones, and Asphalt parking exhibit remarkably low SEM values, indicating high precision in the sample mean estimates. This suggests that the spectral characteristics of these surfaces in the VNIR region are stable and are minimally affected by temporal variations or aging effects. On the other hand, the Polyolefin roof, while maintaining relatively low SEM values, shows slightly more variation compared to the aforementioned surfaces. This variation may imply greater sensitivity to environmental or aging impacts, leading to subtle changes in spectral signatures over time.

Turning to the SWIR bands, surfaces like the aged tiles roof and the new tiles roof display higher SEM values, particularly in the SWIR bands. This suggests greater variability in sample mean estimates over time or increased sensitivity to aging or environmental effects in the SWIR region. The precision differences observed between VNIR and SWIR bands may also stem from the varying spatial resolutions of the WV3 satellite in these spectral regions. The higher spatial resolution in the VNIR bands allows for finer detail capture, potentially enhancing precision in surface characterization and reducing the influence of small-scale variations or aging effects. Conversely, the lower spatial resolution in the SWIR bands may lead to more aggregated or generalized spectral information, which could contribute to increased variability in sample mean estimates, especially for surfaces sensitive to spatial heterogeneity or aging impacts.

It is important to consider these variations when using spectral data for urban analyses, especially for surfaces prone to temporal changes. Despite some surfaces showing increased SEM in the SWIR bands compared to the VNIR bands, they still maintain acceptable levels

of precision. This indicates that despite spectral variations in the SWIR region, sample mean estimates remain reliable for urban analysis purposes.

Table 4. SEM values computed for each ROI and for each band of the WV3 sensor.

ROI *	VNIR								SWIR							
	B1	**B2**	**B3**	**B4**	**B5**	**B6**	**B7**	**B8**	**B9**	**B10**	**B11**	**B12**	**B13**	**B14**	**B15**	**B16**
1	0.003	0.004	0.004	0.004	0.004	0.004	0.005	0.005	0.006	0.007	0.006	0.005	0.006	0.005	0.005	0.004
2	0.001	0.001	0.002	0.003	0.005	0.005	0.006	0.006	0.011	0.018	0.019	0.017	0.022	0.020	0.021	0.019
3	0.001	0.001	0.002	0.003	0.004	0.005	0.005	0.005	0.010	0.010	0.010	0.010	0.009	0.009	0.010	0.008
4	0.001	0.001	0.001	0.001	0.001	0.001	0.001	0.001	0.003	0.003	0.002	0.002	0.005	0.005	0.005	0.004
5	0.000	0.000	0.000	0.001	0.001	0.001	0.001	0.001	0.001	0.001	0.001	0.001	0.001	0.001	0.001	0.001
6	0.000	0.000	0.000	0.000	0.000	0.000	0.000	0.000	0.000	0.001	0.001	0.001	0.001	0.001	0.001	0.001
Min	0.000	0.000	0.000	0.000	0.000	0.000	0.000	0.000	0.000	0.001	0.001	0.001	0.001	0.001	0.001	0.001
Max	0.003	0.004	0.004	0.004	0.005	0.005	0.006	0.006	0.011	0.018	0.019	0.017	0.022	0.020	0.021	0.019
Mean	0.001	0.001	0.001	0.002	0.002	0.003	0.003	0.003	0.005	0.007	0.007	0.006	0.007	0.007	0.007	0.006

* 1: Polyolefin roof, 2: new tiles roof, 3: aged tiles roof, 4: asphalt parking, 5: parking with cobblestones, 6: bituminous membrane.

Therefore, a WV3 image was used for a qualitative and quantitative comparison of surface reflectance spectra for the selected ROIs using statistical parameters. In particular, to assess deviations between the two spectra (simulated and satellite-derived), the RMSE was employed, following the guidelines outlined by Wald [53]. An essential aspect of this comparison process is the temporal interval between the satellite image acquisition in 2018 and the ground measurement campaign in 2023. This time-lapse encompasses the natural aging process experienced by materials, which can significantly affect their characteristics. Unfortunately, simultaneous ground and satellite measurements were not feasible due to temporal constraints. However, addressing this temporal gap and conducting synchronized measurements will be a focal point for future investigations.

The most complete comparison was achieved for the bituminous membrane, as measurements were acquired from the satellite and both ground instruments, i.e., the spectroradiometer and the spectrophotometer.

As illustrated in Figure 7, the spectral signature of this surface, derived from satellite data, was juxtaposed with ground instrument data.

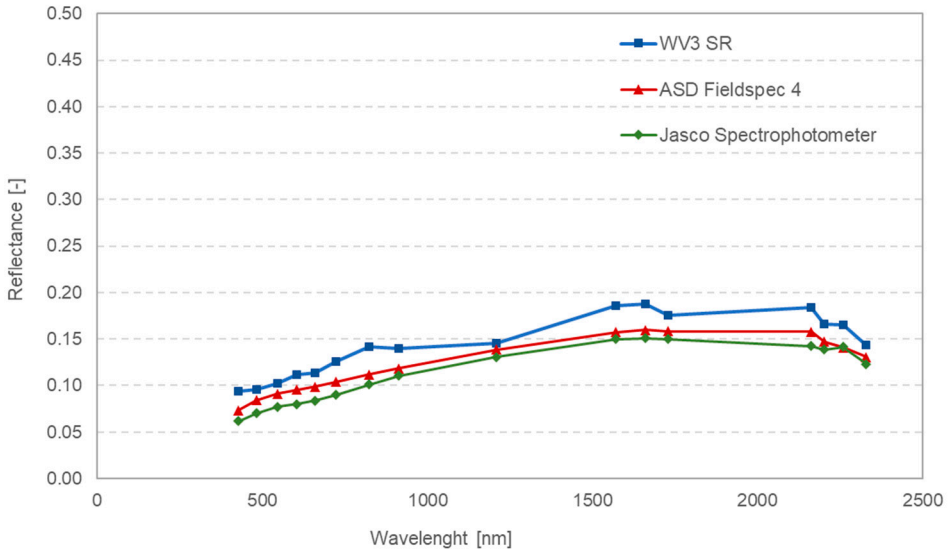

Figure 7. Comparison between the spectral signatures of bituminous membrane achieved by the ASD Fieldspec 4, the Jasco Spectrophotometer, and the resampled WV3 imagery.

Figure 8 presents graphical representations of all six investigated surfaces: the polyolefin roof, the aged and new tiles roofs, the asphalted car park, the bituminous membrane, and the cobblestone parking.

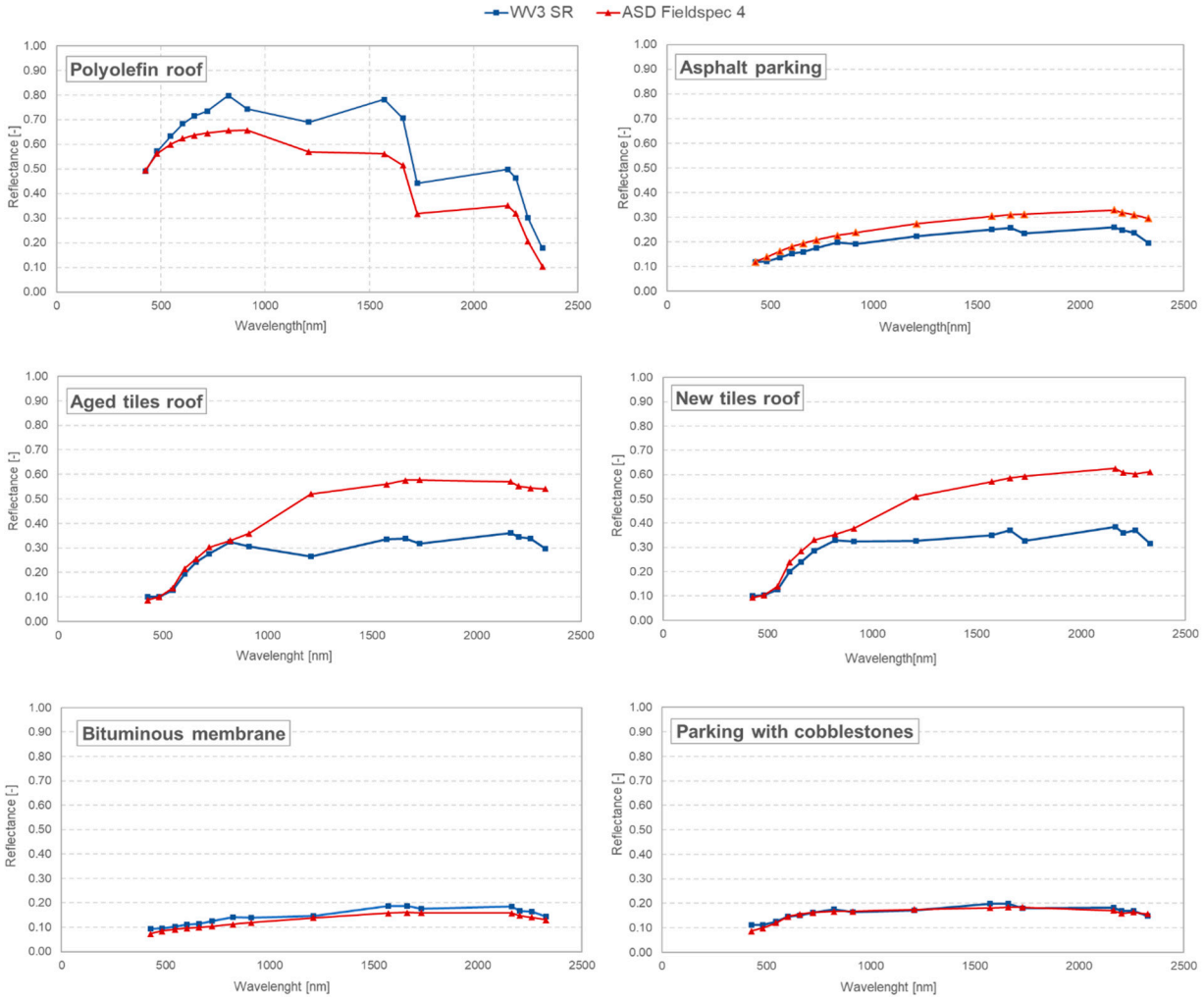

Figure 8. Comparative spectral signature of the six acquired ROI with WV3 Surface Reflectance and ASD Fieldspec 4 measurements resampled with WV3 spectrum.

The spectral resampling of high-resolution spectra acquired using a ground instrument, aimed at simulating the behavior of the WV3 satellite, has yielded promising outcomes despite the temporal gap between the WV3 image acquisition and the ground campaign.

Notably, highly absorbent surfaces, like bituminous membranes, displayed minimal susceptibility to the aging process. The spectra extracted from the satellite image are effectively substitutable with those obtained through instrumental measurement. Similar patterns hold for surfaces with diverse textures, such as car parks paved with cobblestones. For tiled surfaces, the situation is more complicated. Remote sensing characterization faces greater difficulties and is not immediately attainable, primarily due to the evolving nature of the surfaces themselves. More pronounced deviations are evident, particularly within the SWIR spectral region. These deviations can be attributed to the aging process that surfaces undergo over time, and also to the coarse spectral resolution of WV3 in the SWIR region compared to the VNIR. In the case of the Polyolefin roof, the impact of aging becomes apparent. Spectra measured both from the satellite and on-site exhibit a similar trend, albeit with lower reflectance values recorded in 2023. This particular roof is a "cool" white-colored covering, known for experiencing a rapid decline in solar reflectance in the initial years post-application [54]. In this case, ensuring proper surface maintenance becomes fundamental

to mitigate this decline in its reflective properties. Aging effects on the Polyolefin roof are depicted in the spectral measurements, revealing insights into the surface's response to environmental conditions over time. Analogous trends and correlations have been identified in the related literature studies, emphasizing the robustness and reproducibility of our findings across different contexts [55,56].

Table 5 provides an insight into the mean RMSE values computed using the single RMSE values for each WV3 band across each ROI and urban surface type. RMSE serves as a measure of the discrepancy between measured and predicted values, with lower RMSE values indicating higher measurement accuracy. The RMSE values, falling within the 3–4% range, are considered acceptable due to their alignment with the total uncertainty inherent in spectrophotometer/spectroradiometer measurements [16,43]. Among the surfaces analyzed, the "Parking with cobblestones" area stands out for its remarkably low RMSE of 0.01. This suggests a strong agreement between the observed and predicted data, likely because cobblestone surfaces offer a consistent and easily measurable texture. Moving on to the "Bituminous membrane" surfaces, both measurements taken with the ASD Fieldspec 4 and the Spectrophotometer show good agreement with RMSE values of 0.02 and 0.03, respectively. This indicates reliable results from both methods, affirming their effectiveness in assessing bituminous membrane surfaces. The "Asphalt parking" ROI demonstrates a RMSE of 0.06, suggesting a moderate level of accuracy in measurements. Asphalt surfaces typically absorb more solar radiation, contributing to higher urban heat island effects. When comparing the RMSE values for the "Polyolefin roof", "Aged tiles roof", and "New tiles roof" regions, we find them ranging from 0.10 to 0.14. These values indicate a moderate to slightly higher level of deviation, all falling well below the acceptable threshold of 4%. The observed RMSE values suggest a probable influence of aging on surface characteristics.

Table 5. Mean Root Mean Square Error (RMSE) value for each ROI.

ROI	Mean RMSE (-) *
Parking with cobblestones	0.01
Polyolefin roof	0.10
Aged tiles roof	0.13
Asphalt parking	0.06
New tiles roof	0.14
Bituminous membrane (ASD Fieldspec 4)	0.02
Bituminous membrane (Spectrophotometer)	0.03

* The symbol (-) denotes a dimensionless parameter.

Our findings underscore the efficacy of satellite imagery analysis for characterizing homogeneous surfaces like bituminous membranes and cobblestone parking lots. These materials exhibit stable characteristics over time, minimizing the impact of aging on their spectral signatures and allowing image acquisition at any temporal moment. Conversely, surfaces such as brick or cool materials are notably influenced by aging effects, affecting the reliability of satellite-derived characterizations beyond image acquisition.

Hence, materials like bituminous membranes and cobblestone parking lots could potentially be well-characterized using satellite data rather than ground measurements. These surfaces play a pivotal role in effective SUHI mitigation strategies, especially through the strategic application of cool materials. The precision offered by satellite data allows for a comprehensive understanding of these surfaces, enabling targeted interventions to combat the UHI effect and enhance overall urban climate resilience.

3.3. Albedo Analysis

Table 6 showcases a comparison between the solar reflectance (albedo) values obtained through satellite imagery (WV3) on the chosen ROIs and those measured on the ground using the Fieldspec spectroradiometer. Additionally, the ground-measured values have been post-processed to simulate satellite-derived data, aligning with the AM1GH and

E891BN standards. This comparison provides insight into the congruence between ground-based measurements and satellite-derived estimations of solar reflectance.

Table 6. Comparison of solar reflectance: satellite-derived vs. ground-measured.

Urban Surfaces	Solar Reflectance		
	WV3 Satellite	Fieldspec (AM1GH)	Fieldspec (E891BN)
Parking with cobblestones	0.14	0.14	0.15
Polyolefin roof	0.65	0.57	0.58
Aged tiles roof	0.21	0.28	0.32
New tiles roof	0.21	0.30	0.33
Bituminous membrane	0.12	0.11	0.11
Asphalt parking	0.16	0.20	0.22

The comparison of solar reflectance values between satellite-derived data from WV3 and ground measurements using the Fieldspec spectroradiometer, considering the AM1GH and E891BN standards for simulation, reveals interesting patterns across different urban surfaces.

When examining the parking with cobblestones, the solar reflectance values exhibit remarkable consistency across all datasets. This suggests a strong alignment between satellite-derived and ground-measured values for this particular surface type.

In the case of the aged tiles roof, a distinctive trend becomes apparent. The satellite-derived value of 0.21 is noticeably lower than both simulated ground measurements. This discrepancy underscores the role of aging in altering the surface's reflectance characteristics. Similarly, the new tiles roof also showcases the impact of aging on reflectance. The satellite-derived value of 0.21 is lower compared to the simulated ground measurements, reinforcing the idea that aging affects the reflectance properties of this surface type.

For the Bituminous Membrane, the close alignment of values across all datasets (0.12 for the satellite and 0.11 for both simulated ground measurements) suggests a minimal influence of aging on these particular surface's reflectance properties.

Lastly, examining the Asphalt Parking, a significant discrepancy arises. The satellite-derived value of 0.16 is notably lower than the values from simulated ground measurements. This divergence underscores the significance of considering the unique characteristics and conditions of each surface when interpreting reflectance data.

To summarize, the comparative analysis underscores the intricate relationship between satellite-derived observations and simulated ground measurements of solar reflectance values. Various factors, such as aging, surface properties, and measurement standards, contribute to the complexities in reconciling these datasets. However, the results obtained are promising, indicating the potential of satellite-based approaches for this type of characterization. The low RMSE values and minimal differences in albedo for certain surfaces hint at the efficacy and reliability of utilizing satellite data in such analyses. Evidence from albedo comparisons between ground-based and satellite measurements further confirms the trends observed in spectral analyses. WV3 satellite imagery emerges as a reliable substitute for ground-based measurements, especially for homogeneous urban surfaces with low albedo. However, for surfaces affected by aging effects, the timing of image acquisition remains crucial. These findings are consistent with the literature review, where surface albedo has been compared and correlated with ground measurements, especially to validate the satellite product for MODIS or Landsat [57–59].

These findings suggest strategic approaches for UHI mitigation based on satellite data. One recommendation is to leverage satellite imagery for urban surface classification, identifying areas where cool materials can be effectively applied to reduce surface temperatures. For instance, targeting regions with high surface temperatures and low albedo in satellite

images can guide interventions such as the installation of reflective roofing materials or green infrastructure.

Moreover, real-time monitoring using satellites can help track changes in surface properties, guiding maintenance schedules for high-reflectance surfaces to sustain their cooling effects over time. Regular assessments through satellite imagery can also inform urban planners and policymakers about the effectiveness of UHI mitigation strategies, allowing for adaptive measures based on evolving urban heat patterns.

In addition to direct interventions, satellite-based data can support urban planners in developing heat-resilient urban designs. By integrating land surface temperature and albedo data from satellites into urban planning tools, cities can optimize green spaces, building orientations, and material choices to minimize heat absorption and maximize cooling through natural means.

4. Conclusions

The analyses conducted in this study aimed to focus on the phenomenon of SUHI, a phenomenon closely linked to UHI, with a particular emphasis on key parameters such as LST and albedo. To achieve this, we employed satellite imagery from Landsat 5, 7, and 8, as well as by acquiring a WV3 image.

Our analysis of Landsat imagery spanning from 1985 to 2023 revealed a noticeable upward trend in LST across the entire study area during the summer months. Specifically, we observed a significant positive trend of 2.92 °C per decade, demonstrating a consistent and substantial increase in temperature over time.

However, the primary aim of this paper was to endeavor to address these two pivotal questions: "Are satellite remote sensing measurements consistent with ground-based measurements?" and "Can satellite measurements be effectively used to characterize surface conditions, thus replacing laboratory measurements?" Our study places, in fact, a significant emphasis on the comparative analysis between satellite-derived observations and ground-based measurements, particularly focusing on surface reflectance (spectral signature comparison) and albedo values. This comparative analysis serves as a crucial component in assessing the reliability and effectiveness of satellite-based approaches in characterizing surface conditions. Despite inherent complexities arising from factors like surface properties, sensor calibration, and measurement standards, our findings underscore the promising potential of satellite-based analyses.

One important aspect of our investigation is the assessment of RMSE values, which provide insights into the accuracy of satellite-derived data when compared to ground-based measurements. The relatively low RMSE values obtained in our study indicate a favorable level of agreement between the two datasets, suggesting that satellite observations can capture surface characteristics with a reasonable degree of accuracy. This agreement is particularly pronounced on homogeneous surfaces like bituminous membranes and parking lots that show RMSE values lower than 0.03. Interestingly, tile roofs exhibit comparable patterns in the Visible-Near Infrared (VNIR) spectral regions, yet they unveil notable distinctions in the Shortwave Infrared (SWIR) range. Such variations can be attributed not only to the disparate timing of satellite image acquisition in contrast to ground measurement campaigns, but also to the relatively lower resolution of the SWIR bands when compared to the VNIR bands of WV3. These kind of surfaces presents higher values of RMSE ranging from 0.10 to 0.14.

Similar to the results obtained for the RMSE, homogeneous surfaces with high heat absorbance reveal minimal differences in albedo values when comparing satellite-derived data with ground-based measurements. Bituminous membranes, parking with cobblestones, and asphalt parking show differences lower than 0.8, while surfaces more affected by aging problems present values up to 0.12. However, it is important to note that the measured differences between satellite albedo and ground albedo are consistently below 12%, revealing the satellite data's strong capability in surface characterization.

While acknowledging the existing challenges and limitations associated with satellite remote sensing, including issues related to spatial resolution and atmospheric interference, our results highlight the robustness of satellite-based approaches in providing valuable insights into surface conditions. By leveraging the strengths of both satellite and ground-based measurements, researchers can enhance their understanding of UHI dynamics and develop more informed strategies for mitigating the adverse effects of urban heat islands.

Author Contributions: Conceptualization, D.P. and S.T.; methodology, D.P., F.D. and S.C.; validation, M.S. and F.R.; formal analysis, F.D. and S.C.; resources, G.G., M.S. and F.R.; data curation, D.P., S.T., F.D. and S.C.; writing—original draft preparation, D.P., F.D. and S.C.; writing—review and editing, G.G. and S.T. All authors have read and agreed to the published version of the manuscript.

Funding: This work was supported by the "Ecosystem for sustainable transition in Emilia Romagna (ECOSISTER)" project, identified with code ECS_00000033, funded by the European Union NextGenerationEU programme—Call for tender n. 3277 dated 30 December 2021, Award Number: 0001052 dated 23 June 2022—under the National Recovery and Resilience Plan (NRRP) Mission 4, Component 2, 10 Investment Line 1.5: "Establishing and strengthening" of "innovation ecosystems for sustainability", building "territorial leaders of R&D".

Institutional Review Board Statement: Not applicable.

Informed Consent Statement: Not applicable.

Data Availability Statement: The data presented in this study are available on request from the corresponding author. The data are not publicly available due to privacy reasons.

Acknowledgments: The authors extend their gratitude to Alberto Muscio and Chiara Ferrari from EElab at the University of Modena for their assistance with the Jasco V-670 measurements. Additionally, the authors would like to thank the San Giuseppe and Vladimiro Spallanzani schools in Sassuolo for generously allowing us to conduct measurements on their premises.

Conflicts of Interest: The authors declare no conflict of interest.

References

1. Oke, T.R. The heat island of the urban boundary layer: Characteristics, causes and effects. In *Wind Climate in Cities*; Springer: Dordrecht, The Netherlands, 1995; pp. 81–107.
2. Mohajerani, A.; Bakaric, J.; Jeffrey-Bailey, T. The urban heat island effect, its causes, and mitigation, with reference to the thermal properties of asphalt concrete. *J. Environ. Manag.* **2017**, *197*, 522–538. [CrossRef] [PubMed]
3. Oke, T. Urban heat islands. In *The Routledge Handbook of Urban Ecology*; Routledge: London, UK, 2010.
4. Piracha, A.; Chaudhary, M.T. Urban air pollution, urban heat island and human health: A review of the literature. *Sustainability* **2022**, *14*, 9234. [CrossRef]
5. Singh, N.; Singh, S.; Mall, R.K. Urban ecology and human health: Implications of urban heat island, air pollution and climate change nexus. In *Urban Ecology*; Elsevier: Amsterdam, The Netherlands, 2020; pp. 317–334.
6. Iamtrakul, P.; Padon, A.; Chayphong, S. Quantifying the Impact of Urban Growth on Urban Surface Heat Islands in the Bangkok Metropolitan Region, Thailand. *Atmosphere* **2024**, *15*, 100. [CrossRef]
7. Lu, D.; Song, K.; Zang, S.; Jia, M.; Du, J.; Ren, C. The effect of urban expansion on urban surface temperature in Shenyang, China: An analysis with landsat imagery. *Environ. Model. Assess.* **2015**, *20*, 197–210. [CrossRef]
8. Lin, J.; Wei, K.; Guan, Z. Exploring the connection between morphological characteristic of built-up areas and surface heat islands based on MSPA. *Urban Clim.* **2024**, *53*, 101764. [CrossRef]
9. Zeng, P.; Zong, C.; Duan, Z.; Wei, X. Exploring the spatial interplay between built-up environments and surface urban heat island phenomena in the main urban area of Shanghai. *Energy Build.* **2023**, *301*, 113739. [CrossRef]
10. Bretz, S.; Akbari, H.; Rosenfeld, A. Practical issues for using solar-reflective materials to mitigate urban heat islands. *Atmos. Environ.* **1998**, *32*, 95–101. [CrossRef]
11. Rossi, F.; Pisello, A.; Nicolini, A.; Filipponi, M.; Palombo, M. Analysis of retro-reflective surfaces for urban heat island mitigation: A new analytical model. *Appl. Energy* **2014**, *114*, 621–631. [CrossRef]
12. Yang, J.; Pyrgou, A.; Chong, A.; Santamouris, M.; Kolokotsa, D.; Lee, S. Green and cool roofs' urban heat island mitigation potential in tropical climate. *Sol. Energy* **2018**, *173*, 597–609. [CrossRef]
13. Wang, C.; Wang, Z.; Kaloush, K.; Shacat, J. Cool pavements for urban heat island mitigation: A synthetic review. *Renew. Sustain. Energy Rev.* **2021**, *146*, 111171. [CrossRef]
14. Chen, J.; Lu, L. Development of radiative cooling and its integration with buildings: A comprehensive review. *Sol. Energy* **2020**, *212*, 125–151. [CrossRef]

15. Pisello, A.L.; Saliari, M.; Vasilakopoulou, K.; Hadad, S.; Santamouris, M. Facing the urban overheating: Recent developments. Mitigation potential and sensitivity of the main technologies. *Wiley Interdiscip. Rev. Energy Environ.* **2018**, *7*, e294. [CrossRef]
16. Costanzini, S.; Ferrari, C.; Despini, F.; Muscio, A. Standard test methods for rating of solar reflectance of built-up surfaces and potential use of satellite remote sensors. *Energies* **2021**, *14*, 6626. [CrossRef]
17. Levinson, R.; Akbari, H.; Berdahl, P. Measuring solar reflectance—Part I: Defining a metric that accurately predicts solar heat gain. *Sol. Energy* **2010**, *84*, 1717–1744. [CrossRef]
18. Levinson, R.; Akbari, H.; Berdahl, P. Measuring solar reflectance—Part II: Review of practical methods. *Sol. Energy* **2010**, *84*, 1745–1759. [CrossRef]
19. Danner, M.; Locherer, M.; Hank, T.; Richter, K. *Spectral Sampling with the ASD FIELDSPEC 4*; EnMAP Consortium: Potsdam, Germany, 2015.
20. Zhu, Z.; Zhou, Y.; Seto, K.C.; Stokes, E.C.; Deng, C.; Pickett, S.T.; Taubenböck, H. Understanding an urbanizing planet: Strategic directions for remote sensing. *Remote Sens. Environ.* **2019**, *228*, 164–182. [CrossRef]
21. Costanzini, S.; Despini, F.; Beltrami, L.; Fabbi, S.; Muscio, A.; Teggi, S. Identification of SUHI in Urban Areas by Remote Sensing Data and Mitigation Hypothesis through Solar Reflective Materials. *Atmosphere* **2021**, *13*, 70. [CrossRef]
22. Gueymard, C.; Lara-Fanego, V.; Sengupta, M.; Xie, Y. Surface albedo and reflectance: Review of definitions, angular and spectral effects, and intercomparison of major data sources in support of advanced solar irradiance modeling over the Americas. *Sol. Energy* **2019**, *182*, 194–212. [CrossRef]
23. Choudhury, M.A.M.; Marcheggiani, E.; Despini, F.; Costanzini, S.; Rossi, P.; Galli, A.; Teggi, S. Urban tree species identification and carbon stock mapping for urban green planning and management. *Forests* **2020**, *11*, 1226. [CrossRef]
24. Bigi, A.; Ghermandi, G.; Harrison, R.M. Analysis of the air pollution climate at a background site in the Po valley. *J. Environ. Monit.* **2012**, *14*, 552–563. [CrossRef]
25. Sekertekin, A.; Bonafoni, S. Land surface temperature retrieval from Landsat 5, 7, and 8 over rural areas: Assessment of different retrieval algorithms and emissivity models and toolbox implementation. *Remote Sens.* **2020**, *12*, 294. [CrossRef]
26. Teillet, P.M.; Barker, J.L.; Markham, B.L.; Irish, R.R.; Fedosejevs, G.; Storey, J.C. Radiometric cross-calibration of the Landsat-7 ETM+ and Landsat-5 TM sensors based on tandem data sets. *Remote Sens. Environ.* **2001**, *78*, 39–54. [CrossRef]
27. Holden, C.E.; Woodcock, C.E. An analysis of Landsat 7 and Landsat 8 underflight data and the implications for time series investigations. *Remote Sens. Environ.* **2016**, *185*, 16–36. [CrossRef]
28. Wulder, M.A.; Roy, D.P.; Radeloff, V.C.; Loveland, T.R.; Anderson, M.C.; Johnson, D.M.; Healey, S.; Zhe, Z.; Scambos, T.A.; Pahlevan, N.; et al. Fifty years of Landsat science and impacts. *Remote Sens. Environ.* **2022**, *280*, 113195. [CrossRef]
29. Li, L.; Zha, Y.; Wang, R. Relationship of surface urban heat island with air temperature and precipitation in global large cities. *Ecol. Indic.* **2020**, *117*, 113195. [CrossRef]
30. Sharma, R.; Joshi, P.K. Identifying seasonal heat islands in urban settings of Delhi (India) using remotely sensed data–An anomaly based approach. *Urban Clim.* **2014**, *9*, 19–34. [CrossRef]
31. Cook, M.; Schott, J.R.; Mandel, J.; Raqueno, N. Development of an operational calibration methodology for the Landsat thermal data archive and initial testing of the atmospheric compensation component of a Land Surface Temperature (LST) Product from the archive. *Remote Sens.* **2014**, *6*, 11244–11266. [CrossRef]
32. McLeod, A.I. Kendall rank correlation and Mann-Kendall trend test. *R Package Kendall* **2005**, *602*, 1–10.
33. Theil, H. A rank-invariant method of linear and polynomial regression analysis. *Indag. Math.* **1950**, *12*, 173.
34. Panwar, M.; Agarwal, A.; Devadas, V. Analyzing land surface temperature trends using non-parametric approach: A case of Delhi, India. *Urban Clim.* **2018**, *24*, 19–25. [CrossRef]
35. Liu, J.F.; Zhang, X.N.; Wang, H.M. Trend analysis of China flood disaster and challenges in the future. *Appl. Mech. Mater.* **2013**, *405*, 2144–2150. [CrossRef]
36. Cooley, T.; Anderson, G.; Felde, G.; Hoke, M.; Ratkowski, A.; Chetwynd, J.; Lewis, P. FLAASH, a MODTRAN4-based atmospheric correction algorithm, its application and validation. In Proceedings of the IEEE International Geoscience and Remote Sensing Symposium, Toronto, ON, Canada, 24–28 June 2002; pp. 1414–1418.
37. Kuester, M. *Radiometric Use of Worldview-3 Imagery*; Digitalglobe: Oakland, CA, USA, 2016.
38. Thuillier, G.; Hersé, M.; Labs, D.; Foujols, T.; Peetermans, W.; Gillotay, D.; Simon, P.C.; Mandel, H. The solar spectral irradiance from 200 to 2400 nm as measured by the SOLPEC spectrometer from the ATLAS and EURECA missions. *Sol. Phys.* **2003**, *214*, 1–22. [CrossRef]
39. Brivio, P.; Lechi, G.; Zilioli, E. *Principi e Metodi di Telerilevamento*; CittaStudi: Milano, Italy, 2006; pp. 1–525.
40. Parente, C.; Pepe, M. Bathymetry from worldview-3 satellite data using radiometric band ratio. *Acta Polytech.* **2018**, *58*, 109–117. [CrossRef]
41. Munafò, M. *Consumo di Suolo, Dinamiche Territoriali e Servizi Ecosistemici*; Report SNPA; Ispra: Roma, Italy, 2023.
42. Zhang, Y.; Li, D.; Liu, L.; Liang, Z.; Shen, J.; Wei, F.; Li, S. Spatiotemporal characteristics of the surface urban heat island and its driving factors based on local climate zones and population in Beijing, China. *Atmosphere* **2021**, *12*, 1271. [CrossRef]
43. Bonafoni, S.; Keeratikasikorn, C. Land surface temperature and urban density: Multiyear modeling and relationship analysis using MODIS and Landsat data. *Remote Sens.* **2018**, *10*, 1471. [CrossRef]
44. Morabito, M.; Crisci, A.; Messeri, A.; Orlandini, S.; Raschi, A.; Maracchi, G.; Munafò, M. The impact of built-up surfaces on land surface temperatures in Italian urban areas. *Sci. Total Environ.* **2016**, *551*, 317–326. [CrossRef]

45. Wang, S.; Ma, Q.; Ding, H.; Liang, H. Detection of urban expansion and land surface temperature change using multi-temporal landsat images. *Resour. Conserv. Recycl.* **2018**, *128*, 526–534. [CrossRef]
46. Svidzinska, D.; Korohoda, N. Study of spatiotemporal variations of summer land surface temperature in Kyiv, Ukraine using Landsat time series. In *Geoinformatics: Theoretical and Applied Aspects*; European Association of Geoscientists & Engineers: Utrecht, The Netherlands, 2020; Volume 2020, pp. 1–5.
47. Yavaşlı, D.D. Spatio-temporal trends of urban heat island and surface temperature in Izmir, Turkey. *Am. J. Remote Sens.* **2017**, *5*, 24–29. [CrossRef]
48. Tahooni, A.; Kakroodi, A.A.; Kiavarz, M. Monitoring of land surface albedo and its impact on land surface temperature (LST) using time series of remote sensing data. *Ecol. Inform.* **2023**, *75*, 102118. [CrossRef]
49. Bonafoni, S.; Baldinelli, G.; Rotili, A.; Verducci, P. Albedo and surface temperature relation in urban areas: Analysis with different sensors. In Proceedings of the 2017 Joint Urban Remote Sensing Event (JURSE), Dubai, United Arab Emirates, 6–8 March 2017; pp. 1–4.
50. Bossard, M.; Feranec, J.; Otahel, J. *CORINE Land Cover Technical Guide—Addendum*; Technical Report; No. 105; European Enviroment Agency: Copenhagen, Denmark, 2000.
51. Imran, H.M.; Kala, J.; Ng, A.W.M.; Muthukumaran, S. Effectiveness of green and cool roofs in mitigating urban heat island effects during a heatwave event in the city of Melbourne in southeast Australia. *J. Clean. Prod.* **2018**, *197*, 393–405. [CrossRef]
52. Lomba-Fernández, C.; Hernantes, J.; Labaka, L. Guide for climate-resilient cities: An urban critical infrastructures approach. *Sustainability* **2019**, *11*, 4727. [CrossRef]
53. Wald, L. *Data Fusion: Definitions and Architectures: Fusion of Images of Different Spatial Resolutions*; Presses des MINES: Paris, France, 2002.
54. Despini, F.; Ferrari, C.; Santunione, G.; Tommasone, S.; Muscio, A.; Teggi, S. Urban surfaces analysis with remote sensing data for the evaluation of UHI mitigation scenarios. *Urban Clim.* **2021**, *35*, 1–12. [CrossRef]
55. Despini, F.; Ferrari, C.; Bigi, A.; Libbra, A.; Teggi, S.; Muscio, A.; Ghermandi, G. Correlation between remote sensing data and ground based measurements for solar reflectance retrieving. *Energy Build.* **2016**, *114*, 227–233. [CrossRef]
56. Baldinelli, G.; Bonafoni, S.; Anniballe, R.; Presciutti, A.; Gioli, B.; Magliulo, V. Spaceborne detection of roof and impervious surface albedo: Potentialities and comparison with airborne thermography measurements. *Sol. Energy* **2015**, *113*, 281–294. [CrossRef]
57. Lucht, W.; Hyman, A.H.; Strahler, A.H.; Barnsley, M.J.; Hobson, P.; Muller, J.P. A comparison of satellite-derived spectral albedos to ground-based broadband albedo measurements modeled to satellite spatial scale for a semidesert landscape. *Remote Sens. Environ.* **2000**, *74*, 85–98. [CrossRef]
58. Liang, S.; Fang, H.; Chen, M.; Shuey, C.J.; Walthall, C.; Daughtry, C.; Morisette, J.; Schaaf, C.; Strahler, A. Validating MODIS land surface reflectance and albedo products: Methods and preliminary results. *Remote Sens. Environ.* **2002**, *83*, 149–162. [CrossRef]
59. Román, M.O.; Gatebe, C.K.; Shuai, Y.; Wang, Z.; Gao, F.; Masek, J.G.; He, T.; Liang, S.; Schaaf, C.B. Use of in situ and airborne multiangle data to assess MODIS-and Landsat-based estimates of directional reflectance and albedo. *IEEE Trans. Geosci. Remote Sens.* **2013**, *51*, 1393–1404. [CrossRef]